

## Article

# Effect of Aluminum Addition on the Microstructure, Magnetic, and Mechanical Properties of FeCrCoNiMn High-Entropy Alloy

Safia Alleg <sup>1,\*</sup> , Ahlem Bekhouche <sup>1</sup>, Hacene Hachache <sup>1</sup> and Joan Jose Sunol <sup>2</sup> 

<sup>1</sup> Laboratory of Magnetism and Spectroscopy of Solids (LM2S), Department of Physics, Badji Mokhtar Annaba University, B.P. 12, Annaba 23000, Algeria; ahlembekhouche46@gmail.com (A.B.); hachachehacene@gmail.com (H.H.)

<sup>2</sup> Department of Physics, University of Girona, 17003 Girona, Spain; joanjosep.sunyol@udg.edu

\* Correspondence: safia.alleg@univ-annaba.dz or safia\_alleg@yahoo.fr

**Abstract:** High-entropy FeCoCrNiMn (C1) and FeCoCrNiMn<sub>10</sub>Al<sub>10</sub> (C2) alloys (HEAs) were mechanically alloyed for 24 h and heated to 900 °C (C1\_900 °C and C2\_900 °C). The powders were also compacted into pellets (C1\_pellet and C2\_pellet) and sintered at 500 °C for 1 h. Crystal structure, microstructure, magnetic, and mechanical properties were investigated by X-ray diffraction, scanning electron microscopy, vibrating sample magnetometry, and microindentation. During the milling process, a mixture of body-centered-cubic (BCC) and face-centered-cubic (FCC) phases with a crystallite size in the range of 9–13 nm was formed in the C1 HEA alloy. The dual FCC + BCC solid solutions remain for the C1\_pellet and transform to a single FCC for the C1\_900 °C powders. Al addition stabilizes the BCC structure in the FeCoCrNiMn<sub>10</sub>Al<sub>10</sub> HEA alloy, as revealed by the structural refinement. The structure exhibits a mixture of BCC + FCC solid solutions for the C2 powders and BCC + FCC + CrCo sigma phase for the C2\_pellet and C2\_900 °C powders. The crystallite sizes are in the range of 6–93 nm for all the samples. The saturation magnetization ( $M_s$ ), coercivity ( $H_c$ ), and squareness ratio ( $M_r/M_s$ ) are estimated to be 24.2 emu/g, 153.62 Oe, and 0.165, respectively, for C1 and 28.45 emu/g, 188.48 Oe, and 0.172 for C2. The C1\_900 °C and C2\_900 °C powders exhibit, respectively, paramagnetic and soft magnetic behaviors and an exchange bias at room temperature. The C1\_pellet and C2\_pellet HEAs show high hardness values of 584.85 Hv and 522.52 Hv, respectively.

**Keywords:** mechanical alloying; high-entropy alloys; X-ray diffraction; magnetic properties; microstructure; mechanical properties



**Citation:** Alleg, S.; Bekhouche, A.; Hachache, H.; Sunol, J.J. Effect of Aluminum Addition on the Microstructure, Magnetic, and Mechanical Properties of FeCrCoNiMn High-Entropy Alloy. *Crystals* **2023**, *13*, 1483. <https://doi.org/10.3390/cryst13101483>

Academic Editors: Andrey Prokofiev, Andrei Vladimirovich Shevelkov and Chongde Cao

Received: 17 September 2023

Revised: 29 September 2023

Accepted: 10 October 2023

Published: 12 October 2023



**Copyright:** © 2023 by the authors. Licensee MDPI, Basel, Switzerland. This article is an open access article distributed under the terms and conditions of the Creative Commons Attribution (CC BY) license (<https://creativecommons.org/licenses/by/4.0/>).

## 1. Introduction

High-entropy alloys (HEAs), which are defined as alloys with five or more predominant constituent elements, have received significant attention during the last decades due to their excellent mechanical properties, such as high hardness, high ductility, high toughness, suitable oxidation resistance, high thermodynamic stability, excellent wear resistance, and corrosion resistance [1–4]. HEAs are based on an equiatomic multicomponent alloy composed of a disordered solid solution (SS). Random solid solutions prevail over intermetallic compounds due to the high configurational entropy of mixing, which increases with the number of composing elements compared to traditional alloys. Consequently, HEAs provide researchers more freedom to develop new alloys with unusual properties. The processes and chemical composition can affect the phase formation, microstructural evolution, and their relationship with the physical and mechanical properties [5]. HEAs have gained significant attention and are finding use in various industries and applications such as aircraft components, engine components, renewable energy, implantable medical devices, electronics, transportation (high-speed trains), additive manufacturing, etc.

Several preparation methods were utilized to study the impact of the conditions parameters on the microstructure, magnetic, and mechanical properties of multicomponent HEAs alloys such as arc melting [6,7], induction melting [8], mechanical alloying (MA) [9,10], and laser additive manufacturing [11]. In arc melting, high-frequency electric arcs are used to melt and mix the constituent elements rapidly. The molten alloy is then solidified to form the HEA. Arc melting is suitable for bulk production of large and homogeneous ingots. Moreover, induction melting is an effective method for melting and mixing multiple alloying elements to produce HEAs, as it relies on electromagnetic induction to heat and melt materials placed within a crucible or a coil. Induction melting provides better control over temperature and alloy composition. However, mechanical alloying (MA) involves high-energy ball milling of elemental powders to achieve their mixing at the atomic level. The repeated fracturing and cold welding phenomena of the powder particles during the milling process lead to solid-state diffusion and the synthesis of a wide range of HEAs with various compositions such as solid solution, intermetallics, and amorphous alloys. Laser additive manufacturing or selective laser melting (SLM) is well suited for small-batch or prototyping applications since the components are built layer by layer using a high-power laser to selectively melt and fuse metal powder. SLM offers superior control over the microstructure and composition of HEAs and allows for the production of highly complex and customized geometries. The choice of different methods depends on the specific requirements of the HEA application and the available resources and equipment. Depending on the preparation conditions, most alloys consist of multiple phases, including secondary solid solution phases and/or intermetallic compounds [12]. The obtained HEAs with casting techniques from the melt exhibit a single phase, where four or more elements are evenly dispersed in an average ordered, close-packed, and simple crystalline structure, forming a random solid solution [11,12]. The high chemical disorder within the unit cell introduces disorder at a larger scale due to the random atomic arrangement within the unit cell. However, owing to the differences in local atomic configuration, the diffusion of atoms is slower in multicomponent alloys compared to binary alloys. Furthermore, due to atomic radii difference, the lattice distortions influence the solid solution formation.

The equiatomic FeCoCrMnNi system alloy, known as the Cantor alloy, exhibits a single face-centered-cubic (FCC) solid solution (space group Fm-3m and lattice parameter  $a = 3.3605 \text{ \AA}$ ), high ductility (50–60%), reasonable strength (yield strength = 160 MPa), and toughness ( $>217 \text{ MPa m}^{1/2}$ ) at room temperature [13,14]. Nevertheless, the single-phase microstructure and low lattice distortion restricted the application of this alloy due to the lack of sufficiently low yield and ultimate tensile strength [15]. The strength of the FCC phase can be improved through microstructural changes by adding some elements to the FeCoCrMnNi HEA alloy, such as aluminum (Al), which forms bonds with other metals and affects the microstructure. Moreover, Al addition leads to solid solution hardening and strength improvement due to its larger atomic radius ( $r_{\text{Al}} = 0.143 \text{ nm}$ ) compared to other metallic Fe ( $r_{\text{Fe}} = 0.124 \text{ nm}$ ), Co ( $r_{\text{Co}} = 0.125 \text{ nm}$ ), Cr ( $r_{\text{Cr}} = 0.128 \text{ nm}$ ), Mn ( $r_{\text{Mn}} = 0.135 \text{ nm}$ ), and Ni ( $r_{\text{Ni}} = 0.125 \text{ nm}$ ) elements. The solid solution strengthening occurs through the dispersion of the Al atoms within the crystal lattice, leading to lattice distortions and increasing the resistance of dislocation motion. The presence of Al in the HEAs can also affect the alloy microstructure (grain size, phase distribution, and grain boundaries), corrosion resistance, and mechanical and thermal properties. However, Al may also reduce the ductility and toughness, particularly at high content. Furthermore, due to its relatively low density, the addition of Al to HEAs can be helpful in applications where weight reduction is required, such as aerospace and transportation. It is important to note that the specific effects of Al in HEAs can vary widely depending on the other elements present in the alloy and their relative proportions [16–22].

It has been reported that dual-phase (FCC + BCC) HEAs possess a superior balance of strength and ductility compared to the single FCC structure. Among those HEAs, the AlFeCoCrNi HEA system is one of the most widely studied dual-phase HEAs, as Al addition significantly affects phase formation and microstructural evolution [16–19]. Indeed, Al can

dissolve in the FCC phase and expand the lattice up to 6 at.%, causing lattice distortion and leading to a monotonous increase in hardness. For higher Al amounts (6–10 at.%), (Al, Ni, Fe)-rich B2 phase precipitates in the FCC matrix with nearly spherical shape and nanometric size, causing a rapid increase in the hardness [19]. The literature reports on  $Al_xCoCrFeNi$  suggest that the alloy exhibits a phase transition between FCC, FCC + BCC, and BCC as a function of Al content [20,21]. It has been reported that AlCoCrFeNi alloy presents a simple BCC phase, while the FCC structure increases in the AlCoCrFeNi $_x$  ( $x \geq 1.5$ ). Al and Ni elements are enriched in the BCC phase, while Co, Cr, and Fe elements are enriched in the FCC phase [22]. The microstructure of solidified HEA AlCoCrFeNi showed dendritic and interdendritic morphologies owing to elemental segregation. The dendritic segregation area was Al, Ni-rich, and Cr, Fe depleted, while the interdendritic segregation area was Cr, Fe-rich, and Al, Ni depleted. However, the distribution of Co was uniform [23]. However, a separation into a B2 Al–Ni-rich matrix and bcc Cr–Fe-rich precipitates can be observed in dendritic and interdendritic regions [24,25].

The present work aims to study the effect of Al addition on the phase formation, microstructure, and magnetic properties of the mechanically alloyed CoCrFeNiMn HEAs for 24 h using X-ray diffraction (XRD), scanning electron microscopy (SEM) coupled with energy-dispersive X-ray spectroscopy (EDS), and vibrating sample magnetometer (VSM). The replacement of 0.1 Mn by 0.1 Al can be related to the fact that: (i) Al is much lighter than Mn, which can be advantageous in applications such as aerospace and automotive applications; (ii) Al is known for its corrosion resistance; (iii) Al addition can improve the electrical conductivity of HEAs, making them suitable for electrical applications, and is more readily available and cost-effective compared to Mn. To better understand the effect of Al addition on the phase stability and mechanical properties, the mechanically alloyed powders are subjected to a continuous heat treatment to 900 °C in a differential scanning calorimeter (DSC) and also compacted into pellets and sintered at 500 °C for 1 h. Microindentation tests are used to determine the microhardness.

## 2. Materials and Methods

MA was used to prepare equiatomic FeCoCrNiMn and FeCoCrNiMn $_{10}$ Al $_{10}$  (wt. %) high-entropy alloys, named hereafter C1 and C2, respectively. The alloys were prepared from elemental powders of Fe (6–8  $\mu$ m, 99.5% purity), Co (1.6  $\mu$ m, 99.8% purity), Cr (<15  $\mu$ m, 99% purity), Ni (3–7  $\mu$ m, 99.9% purity), Mn (6–8  $\mu$ m, 99.3% purity), and Al (<15  $\mu$ m, 99.5% purity) in a high-energy planetary ball mill Fritsch P7, under an argon atmosphere, using hardened steel balls and vials. The milling process was performed for 24 h, with a powder-to-ball weight ratio of 1/8 and a rotation speed of 500 rpm. To prevent the increase in the temperature inside the vials, the milling process was interrupted for 15 min after 15 min of milling.

The mechanically alloyed C1 and C2 powders were subjected to continuous heating in the temperature range of 25–900 °C, at a heating/cooling rate of 10 °C/min utilizing a differential scanning calorimeter (DSC, Labsys1600 °C, Setaram, Caluire-et-Cuire, France). The heat-treated powders are named hereafter C1\_900 °C and C2\_900 °C, respectively. The C1 and C2 powders were then compacted into pellets of 13 mm in diameter and 2 mm in thickness using a Specac manual press with 12 tons. The pellets were sintered at 500 °C for 1 h in a Nabertherm L189 tubular furnace (GmbH Bahnhofstr, Berlin, Germany) and cooled down in the furnace. The sintered pellets are labeled hereafter C1\_pellet and C2\_pellet, respectively.

X-ray diffraction (Malvern PANalytical Ltd., Malvern, UK) was used to investigate the phase formation by a PANalytical Empyrean diffractometer configured in a ( $\theta$ – $\theta$ ) Bragg Brentano geometry with Cu-K $\alpha$  radiation ( $\lambda = 1.540598$  Å), a scan range of (30–100)°, and a step size of 0.13°/min. The morphology was examined by a scanning electron microscope (SEM, VEGAS3 TESCAN) (TESCAN, Brno, Czech Republic) combined with energy-dispersive X-ray spectroscopy (EDS) (Bruker Nano GmbH, Berlin, Germany). The magnetic parameters of the C1, C2, C1\_900 °C, and C2\_900 °C powders (saturation mag-

netization,  $M_s$ , coercivity,  $H_c$ , and saturation to remanence (or squareness) ratio,  $M_r/M_s$ ) were determined by a vibrating sample magnetometer (Lakeshore Model 7404, Westerwille, OH, USA) in an external magnetic field of 15 kOe. A Zwick/Roell microindenter (GmbH & Co. KG, Eschwege, Germany) was used to determine the microhardness of the C1\_pellet and C2\_pellet under 5 N load and 10 s dwell time. At least ten measurements were carried out for each sample to obtain statistically relevant values.

### 3. Results

#### 3.1. Phase Formation

MA is a solid-state reaction method for the preparation of nanocrystalline materials with uniform microstructures and compositional homogeneity through particle size reduction, grain size refinement down to the nanometer scale, mixing, blending, and reshaping of the particles. MA is a non-equilibrium process for powder processing of alloys containing low/high melting point elements. During the milling process, the powder particles are trapped between the balls and/or in the ball-wall surface, leading to deformation, fracture, welding, and rewelding that depends on the nature of the metallic powders. The total mixing of the elemental powders at the atomic level is evidenced by the disappearance of their diffraction peaks, as shown by the XRD patterns of the mechanically alloyed C1 and C2 powders for 24 h in Figure 1. Moreover, the broadening of the diffraction peaks and the decrease in their height are related to the crystallite size reduction and the introduction of an important fraction of structural defects during the milling process, such as vacancies, grain boundaries, dislocations, and so on. Likewise, the peak asymmetry can be related to the structural heterogeneity through the existence of more than a single solid solution. Furthermore, the effect of Al addition is revealed by the shape and position of the main diffraction peak. Accordingly, the phase identification was determined using the MAUD program [26], which is based on the Rietveld method [27]. The structural refinement was achieved with two phases: Cr-type BCC (lattice parameter  $a_0 = 2.884 \text{ \AA}$ , space group  $Im - 3m$ ), and Ni-type FCC (lattice parameter  $a_0 = 3.528 \text{ \AA}$ , space group  $Fm - 3m$ ). For the HEAs, the formation of disordered solid solutions during the milling process is allowed by the proximity of the atomic radii of the constituent components Al, Cr, Fe, Mn, Co, and Ni ( $r_{Al} > r_{Mn} > r_{Cr} > r_{Co} = r_{Ni} > r_{Fe}$ ), their large negative enthalpies of mixing, and their activation energies (Table 1). The misfit in the mixing enthalpy of the constituent elements affects the configurational entropy of a random solid solution. Moreover, the higher the magnitude of the mixing enthalpy of binaries scales, the more probable the local chemical short-range order. Hence, to obtain a random solid solution, it is important to minimize both the magnitude and fluctuation in the mixing and formation enthalpy associated with a multicomponent alloy because the enthalpy acts like “resistance” against the random solid solution formation. This disagrees with the higher configurational entropy, which favors random solid solution over other phases.

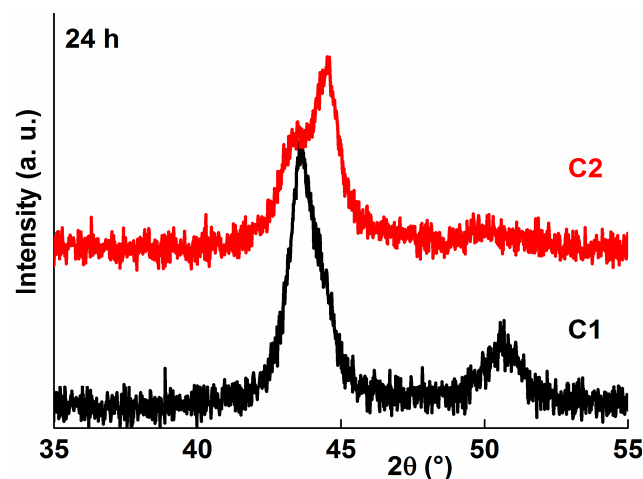


Figure 1. XRD patterns in the  $2\theta$  range of  $(35\text{--}55)^\circ$  of the milled C1 and C2 powders for 24 h.

Table 1. Characteristics of the starting Al, Cr, Mn, Fe, Co, and Ni elements: atomic radii, valence electron. Concentration (VEC), melting temperature, crystal structure, activation energy (Q) [28], and enthalpies of mixing for binary pairs of the multicomponent alloy ( $\Delta H_{\text{mix}}$ ) [29].

Element	Al	Cr	Mn	Fe	Co	Ni
Atomic radii (nm)	0.143	0.128	0.135	0.124	0.125	0.125
VEC	3	6	7	8	9	10
Melting temperature (K)	933	2180	1358	1811	1768	1728
Crystal structure	FCC	BCC	Complex cubic	BCC	HCP	FCC
Activation energy (kJ/mol)	210.4	313	272	309	270	304
$\Delta H_{\text{mix}}$ Al (kJ/mol)	-----	−10	−19	−11	−19	−22
$\Delta H_{\text{mix}}$ Cr (kJ/mol)	−10	-----	−9	−1	−4	−7
$\Delta H_{\text{mix}}$ Mn (kJ/mol)	−19	−9	-----	0	−5	−8
$\Delta H_{\text{mix}}$ Fe (kJ/mol)	−11	−1	0	-----	−1	−2
$\Delta H_{\text{mix}}$ Co (kJ/mol)	−19	−4	−5	−1	-----	0
$\Delta H_{\text{mix}}$ Ni (kJ/mol)	−22	−7	−8	−2	0	-----

Crystal structures, lattice parameters, average crystallite sizes, root-mean-square (r.m.s) microstrains, and weight fractions are summarized in Table 2. The presence of BCC and FCC solid solutions in the FeCoCrNiMn is different from those obtained earlier [13–15], where it has been reported that the crystal structure consists of a single FCC phase. Those discrepancies can be attributed mainly to the preparation conditions. Indeed, a single-phase FCC solid solution was obtained after 20–40 h in the mechanically alloyed CrMnFeCoNi using a planetary ball mill (RETSCH PM-400), a ball-to-powder ratio of 10:1, and a rotation speed of 400 rpm [30]. Moreover, it has been reported that the FeCoCrNiMn HEA prepared by arc melting followed by homogenization for 48 h at 1200 °C exhibited a single FCC structure due to the great configurational entropy and small misfit in the mixing enthalpy. Furthermore, the FCC structure was stable by long-term annealing at 900 °C but became thermodynamically unstable at intermediate temperatures of 700 °C and 500 °C [31]. The formation of stable solid solutions in the HEAs alloys is due to low Gibbs free energy ( $\Delta G$ ), resulting in a high entropy of mixing ( $\Delta S_{\text{mix}}$ ). The phase's stability in HEAs can be affected by changes in composition. For example, the addition of Al to the CrMnFeCoNi alloy promotes a BCC structure over FCC one. In the composition range of 8 at% < Al < 16 at%, Al addition leads to a change from FCC to a mixture of FCC and BCC, while a single BCC phase is obtained for higher Al content [32]. Usually, the addition of a new element to a

multicomponent system leads to much larger thermodynamic changes, which depend on the type of the element added. For example, CoCrFeNiAl and CoCrFeNiMn have similar configurational entropies but are significantly different in their properties and structures, which are predominantly BCC and exclusively FCC, respectively [33]. The type of solid solution (BCC, FCC, or BCC + FCC) in the HEAs can be controlled by the valence electron concentration (VEC). Hence, a BCC solid solution can be formed with a VEC lower than 6.87, FCC with a VEC higher than 8, and a mixture of BCC + FCC with a VEC in the range of 6.87–8. It seems that the proposed criterion to predict the formation of a single FCC solid solution [33] is not valid for the C1 powders, although the VEC is equal to 8. This means that the crystal structure and phase formation can be influenced by other parameters, mainly in the MA process.

**Table 2.** Lattice parameter,  $a$ , relative deviation,  $\Delta a$ , crystallite size,  $\langle L \rangle$ , r.m.s microstrains, and weight fractions obtained from the Rietveld refinement of the XRD patterns of the ball-milled C1 and C2 HEAs for 24 h.

Sample	Structure	$a \pm 10^{-4}$ (Å)	$\Delta a$ (%)	$\langle L \rangle \pm 1$ (nm)	r.m.s (%)	Weight Fraction $\pm 1$ (%)
C1	BCC-SS	2.8878	0.13	9.0	0.18	11.0
	FCC-SS	3.5948	1.89	13.0	0.39	89.0
C2	BCC-SS	2.8822	−0.06	9.9	0.01	68.0
	FCC-SS	3.6221	2.66	9.2	0.46	32.0

According to the Hume–Rothery rules, the formation of BCC- and/or FCC-disordered solid solutions could be based on the atomic radii difference, which plays an important role in the stability and phase formation of multicomponent systems [34]. This means that the: (i) atom size difference among the constituent elements must be less than ~15%; (ii) electronegativity difference must be small; and (iii) VEC numbers of the constituent elements must be similar. When the atomic radii of two elements are similar, they are more likely to form metallic or covalent bonds, and electronegativity is a measure of an element's ability to attract electrons in a chemical bond. The VEC number is valuable for predicting the crystal structures of compounds. Nevertheless, these rules mean that any misfit in the physical/chemical properties of the constituent elements of an alloy is not in favor of a random solid solution. He et al. have suggested the idea of entropic stabilization in connection with the Hume–Rothery rules through the potential energy fluctuation (PEF) model [35]. The notion of entropy stabilization involves increasing disorder within a material to stabilize a specific structure. It should involve the following measures: (1) to increase the number of elements, (2) to minimize all sorts of property misfits (atomic size, chemical bond, etc.), and (3) to maximize the melting temperature. By increasing the number of constituent elements, the configurational entropy of the system increases because the material has more ways to distribute its constituent atoms, enhancing the disorder at higher temperatures. Moreover, alloying elements with different properties leads to stress/strain and induces the formation of ordered structures, which are usually less entropically favored. Thus, selecting elements with similar properties reduces the stress, enhances the disorder, and minimizes property misfits. Finally, by maximizing the melting temperature, the material may remain in a more disordered and higher-entropy state at elevated temperatures. For the equiatomic CoCrFeMnNi, the atom difference size is  $\delta = 3.27$ . The average melting point is about 1801 K, and the correlated entropy  $S_{\text{corr}}/k_B = 1.5668$  [36]. In a multicomponent alloy, the atomic size misfit can be quantified by the well-known  $\delta$  parameter using the following equation [37]:

$$\delta = 100 \sqrt{\sum_{i=1}^n c_i \left(1 - \frac{r_i}{\bar{r}}\right)^2} \quad (1)$$

where  $n$  is the number of components,  $\bar{r} = \sum c_i r_i$ , is the average atomic radius,  $c_i$  and  $r_i$  are the atomic percentage and atomic size of the  $i$ th element, respectively;  $\delta > 0$  corresponds to the reduction in the overall atom size, and  $\delta < 0$  corresponds to the increase in the overall atom size. Thus, the smaller  $\delta$  parameter ( $1\% \leq \delta \leq 5\%$ ) favors the random solid solution formation in HEAs, while ordered solid solution forms in the region of  $5\% \leq \delta \leq 6.6\%$  [38]. Accordingly, the solid solution formation in the C1 and C2 alloys agrees well with the  $\delta$  parameter values of C1 ( $\delta = 3.16$ ) and C2 ( $\delta = 4.63$ ).

The lattice parameter of the BCC solid solution in the mechanically alloyed C1 powders ( $a = 2.8878 \text{ \AA}$ ) is slightly higher than that of the C2 ( $a = 2.8822 \text{ \AA}$ ), and their relative deviations are of about 0.13% and  $-0.06\%$ , respectively. The small expansion/contraction of the crystal lattice can be related to the slight misfit in the atomic radii of the elemental powders. Moreover, the lattice parameter of the FCC solid solution of the C1 powders ( $a = 3.5948 \text{ \AA}$ ) is lower than that of the C2 powders ( $a = 3.6221 \text{ \AA}$ ), and their relative deviations reach as much as 1.86% and 2.66%, respectively. The significant increase in the lattice parameter of the FCC solid solution for the C2 powders can be related to the aluminum addition with a larger atomic radius (0.143 nm) compared to the other elements. The lattice distortion of the two solid solutions might be attributed to the severe plastic deformation that introduces many types of structural defects and an increase in their density during the milling process. Likewise, the significant lattice distortion of the FCC solid solution can be due to the nature of the starting powders, particularly the ductility of Ni and Al, and the lower fusion temperature of aluminum (660 °C).

The crystallite size of C2 powders is almost identical for FCC and BCC solid solutions (9.2–9.9 nm) but varies slightly for the C1 alloy (9–13 nm). Moreover, the r.m.s microstrains, which are more important for the FCC than BCC solid solutions, agree well with the crystal lattice distortion. The microstructure of HEAs may be affected by many factors, such as high entropy, severe lattice distortion, sluggish diffusion, and cocktail effects [39]. The weight fraction of the BCC solid solution, which may include both A2 and B2 structures, increases from 11% for C1 to 68% for C2 alloy. Simultaneously, the weight fraction of the FCC solid solution decreases from 89% for C1 to 32% for C2 alloy. Al addition is evidenced by the increase in the weight fraction of the BCC solid solution for the C2 alloy. Indeed, although aluminum has an FCC structure, it acts as a strong BCC stabilizer, and its addition enhances the strength of the alloy at the cost of reduced ductility. The increase in the BCC weight fraction with aluminum addition is in suitable agreement with the reported results earlier in the literature [33].

Figure 2 displays the XRD patterns of the sintered C1\_pellet and C2\_pellet for 1 h at 500 °C. The alloys exhibit different structures, as confirmed by the shape, height, and position of the diffraction peaks. Those observations are related to the crystal structure changes upon sintering. The XRD pattern of the C1\_pellet shows a single, fine, intense, and asymmetric main diffraction peak situated at about  $2\theta = 44.65^\circ$ . One also observes a shift of the diffraction peaks toward higher  $2\theta$  angles (inset in Figure 2). The variation in the height and width of the diffraction peak can be linked to the crystallite size growth, recovery, internal level strains, and structural defect reduction. Nevertheless, the XRD pattern of the sintered C2\_pellet presents the same shape as that of the milled powders for 24 h but shows an important reduction in the peak's height and a slight shift toward smaller  $2\theta$  angles. Accordingly, the Rietveld refinement of the XRD patterns (Table 3) shows that the crystal structure of the C1\_pellet is a mixture of BCC and FCC structures, while that of the C2\_pellet reveals the formation of tetragonal sigma  $\text{Cr}_{0.528}\text{Co}_{0.472}$  phase ( $a_0 = b_0 = 8.75 \text{ \AA}$ ,  $c_0 = 4.54 \text{ \AA}$ , and space group P42/mnm) in addition to the BCC and FCC structures.

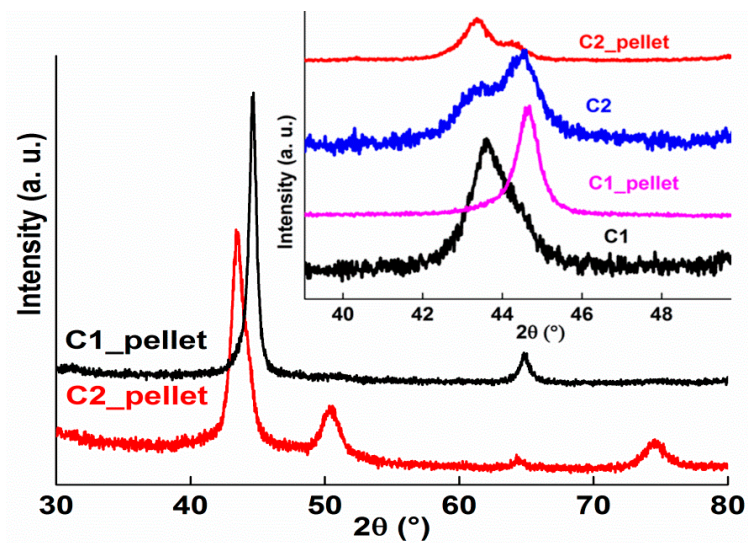


**Figure 2.** XRD patterns of the sintered C1\_pellet and C2 pellet for 1 h at 500 °C. The inset shows the comparison of the main diffraction peak of the powders and pellets.

**Table 3.** Lattice parameters,  $a$ , crystallite size,  $\langle L \rangle$ , r.m.s microstrains, and weight fractions of the sintered C1\_pellet and C2\_pellet for 1 h at 500 °C.

Sample	Structure	$a \pm 10^{-4}$ (Å)	$c \pm 10^{-4}$ (Å)	$\langle L \rangle \pm 1$ (nm)	r.m.s (%)	Weight Fraction $\pm 1$ (%)
C1	BCC-SS	2.8778	----	50.0	0.46	17.8
	FCC-SS	3.5984	----	14.8	0.39	82.2
C2	BCC-SS	2.8853	----	77.6	0.42	16.13
	FCC-SS	3.6099	----	16.7	0.39	78.54
	$\sigma$ -CrCo	8.8955	4.6011	5.8	0.35	5.33

The phase stability of the mechanically alloyed powders was investigated by DSC at continuous heating to 900 °C, as shown in Figure 3. The DSC curves of the C1 and C2 powders reveal the presence of exothermic peaks in the temperature range of 324–700 °C. One notes also that the heat flow is more important for the C2 powders. According to the above XRD results of the sintered pellets at 500 °C, the first exothermic peak can be attributed to recovery, crystallite growth, structural changes, and/or atomic reorganization. Further heating to higher temperatures leads to phase transformations, as revealed by the difference in the XRD patterns of the C1\_900 °C and C2\_900 °C powders (Figure 4). Hence, the XRD pattern of the C1\_900 °C powders displays a set of narrow, intense, and symmetric diffraction peaks attributable to a single FCC solid solution. However, the presence of new diffraction peaks for the C2\_900 °C powders is ascribed to the formation of the sigma phase. Accordingly, the best Rietveld refinement of the XRD patterns (Figure 5) was achieved with a single FCC solid solution for the C1\_900 °C alloy (Figure 5a), and a mixture of BCC, FCC, and tetragonal sigma  $\text{Cr}_{0.528}\text{Co}_{0.472}$  phase for the C2\_900 °C alloy (Figure 5b). It is well known that both Co and Ni elements stabilize the FCC phase at moderate and elevated temperatures and suppress the formation of the brittle  $\sigma$  precipitates, whereas Cr, Fe, and Mn elements promote its formation [40]. The sigma phase, which is commonly observed in aged HEAs [41–43], is a Cr-rich intermetallic compound based on a tetragonal unit cell containing 30 atoms. The formation of  $\sigma$  in the CoCrFeNi HEA [41] has been attributed to the atomic radius difference ( $\delta$ ), VEC concentration, and paired sigma-forming element (PSFE) content. Moreover, the alloying of Al improves the formation of the sigma phase in the HEAs [44]. The formation of the  $\sigma$  phase appears to be a quinary variant of the binary  $\sigma$  phase and may be related to the fact that Cr is a strong  $\sigma$  phase former. The  $\sigma$  phase is well known to form in the binary systems Cr-X type where X = Co, Fe, Mn, and Ni [42,43,45].

It is thus possible that a quinary  $\sigma$  phase containing Cr, Co, Fe, Mn, and Ni elements can also form. Moreover, despite being stable over different compositional domains, the lattice parameters of the reported binary Cr-X  $\sigma$  phases were very comparable due to the similarity in their atomic radii. Consequently, one might expect these atoms to substitute for each other without making the sigma phase unstable.

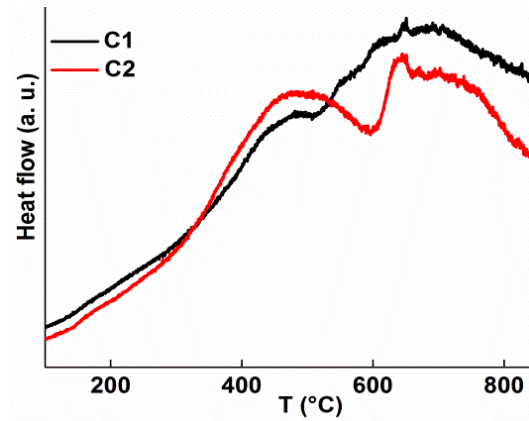


Figure 3. DSC curves of the ball-milled C1 and C2 powders for 24 h.

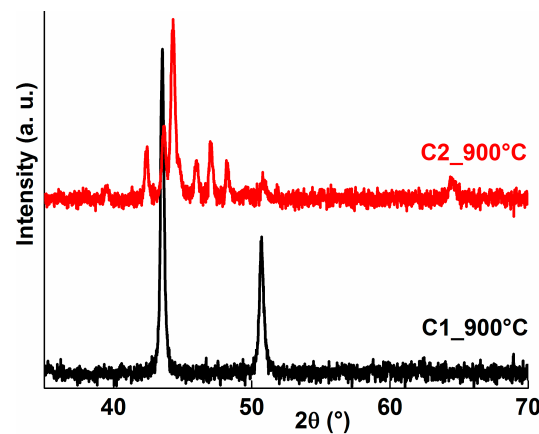


Figure 4. XRD patterns of the heat-treated C1 and C2 powders in the DSC.

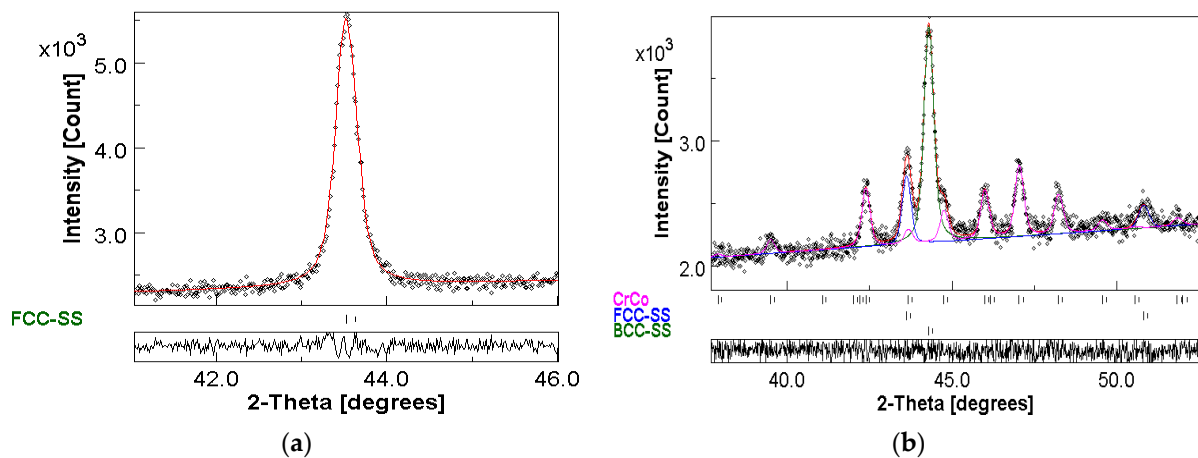


Figure 5. Rietveld refinement of the XRD patterns of the C1<sub>900 °C</sub> and C2<sub>900 °C</sub> samples taken in the 2-theta range of (35–55)° for: (a) C1<sub>900 °C</sub> alloy; and (b) C2<sub>900 °C</sub> alloy.

The lattice parameters, average crystallite size, root-mean-square (r.m.s) microstrains, and weight fractions are assembled in Table 4. The continuous heating/cooling leads to an important increase in the crystallite size to about 63–93 nm for all the structures. Moreover, the BCC structure transforms completely to FCC structure for the C1\_900 °C powders, while its weight fraction reduces to 33.9% for the C2\_900 °C powders. Likewise, the weight fraction of the FCC structure decreases from 32% for the milled powders to 13.5% after the heat treatment. The slight increase in the lattice parameters of the FCC and BCC structures of C1\_900 °C and C2\_900 °C powders, respectively, can be related to the atomic reorganization through the dissolution of aluminum with a larger atomic radius. Likewise, the decrease in the lattice parameter of the FCC structure of C2 from 3.6221 to 3.5909 Å can be attributed to strain relaxation and recovery. The fact that the lattice parameter of the FCC solid solution is comparable for C1\_900 °C ( $a = 3.5987$  Å) and C2\_900 °C ( $a = 3.5909$  Å) might be due to the composition closeness of both solid solutions.

**Table 4.** Lattice parameters ( $a$ ,  $c$ ), crystallite size,  $\langle L \rangle$ , r.m.s microstrains, and weight fractions obtained from the Rietveld refinement of the XRD patterns of C1\_900 °C and C2\_900 °C powders.

Sample	Structure	$a \pm 10^{-4}$ (Å)	$c \pm 10^{-4}$ (Å)	$\langle L \rangle \pm 1$ (nm)	r.m.s (%)	Weight Fraction $\pm 1$ (%)
C1_900 °C	FCC-SS	3.5987	----	72.0	0.09	100
C2_900 °C	BCC-SS	2.8896	----	63.5	0.14	33.9
	FCC-SS	3.5909	----	81.0	0.13	13.5
	$\sigma$ -CoCr	8.7953	4.5588	93.0	0.11	52.6

### 3.2. Morphology

Figure 6a shows typical images of the mechanically alloyed C1 and C2 powders for 24 h and their corresponding ponctual EDS analyses. The powder particles exhibit different shapes and sizes. Additionally, the existence of smaller and bigger particles, ranging from 5 to 40  $\mu\text{m}$  for C1 and from 1 to 55  $\mu\text{m}$  for C2 powders, is due to the competition between fracturing and cold welding during the milling process. The elemental analyses reveal that each particle contains the initial Cr, Mn, Fe, Co, and Ni elements for the C1 powders. However, this is not the case for the C2 powders, where the heterogeneity of the particles is evidenced by the fluctuation of the composition from region to region. The presence of Cr-rich particles with about 98.81 and 98.33 wt. % for points 1 and 4, respectively, might explain the formation of the  $\sigma$ -CoCr phase in the C2\_900 °C powder as revealed by the structural analysis.

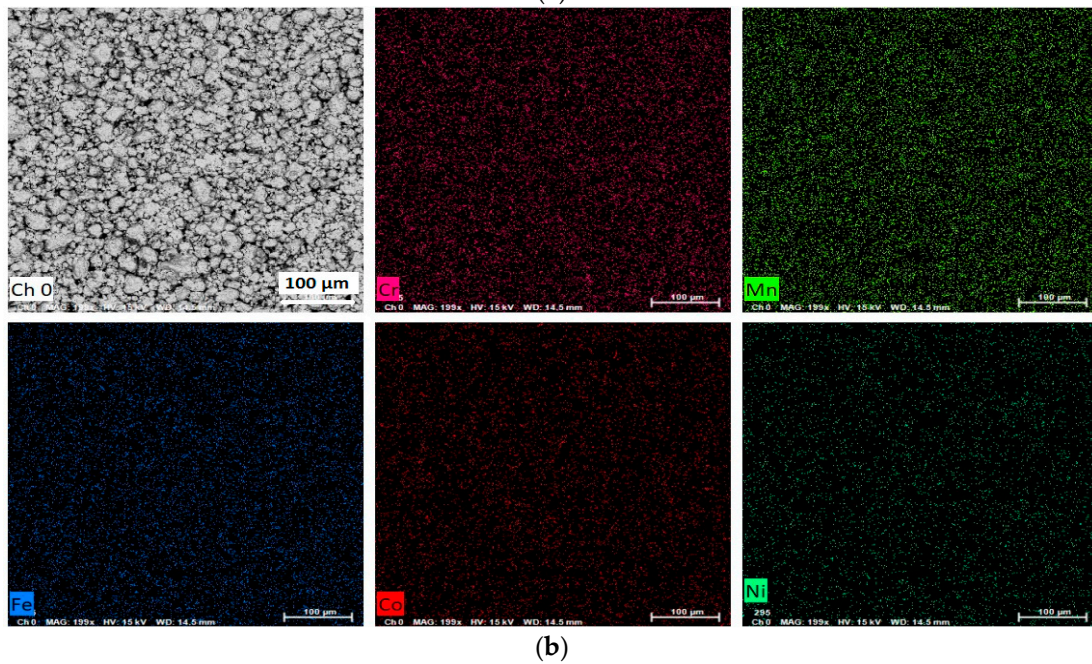
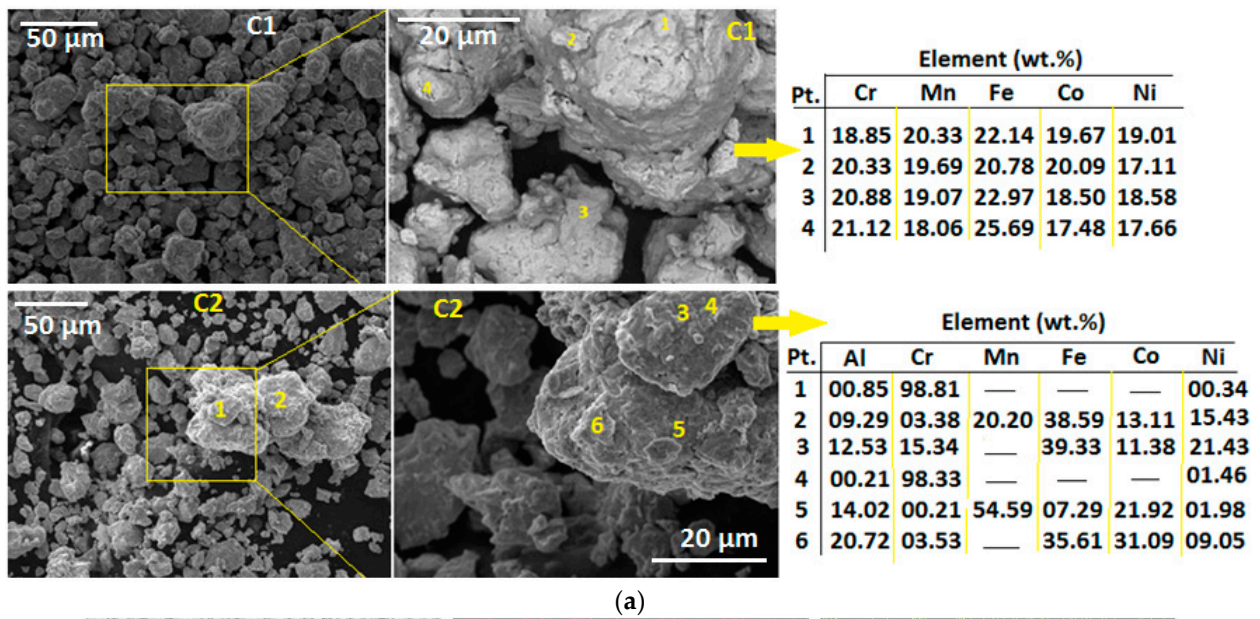
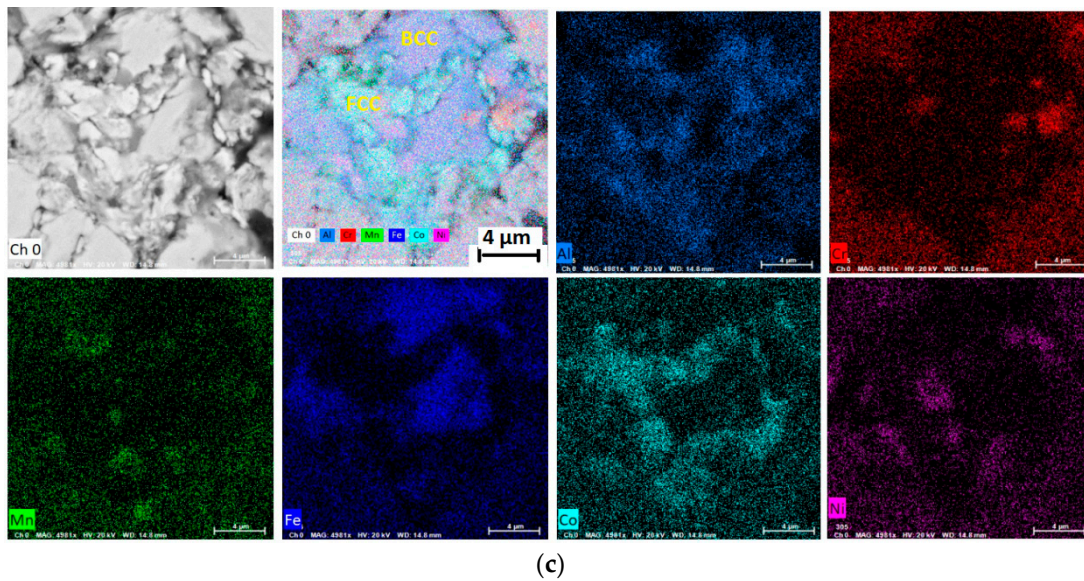


Figure 6. Cont.



**Figure 6.** (a) Typical SEM microstructure showing particles ranging from 5 to 40  $\mu\text{m}$  for C1 and 1 to 55  $\mu\text{m}$  for C2 powders. The tables summarize the EDS point analysis for the C1 and C2 powders; (b) SEM images and EDS element maps of the sintered C1\_pellet for 1 h at 500  $^{\circ}\text{C}$ ; (c) SEM images and EDS element maps of the sintered C2\_pellet for 1 h at 500  $^{\circ}\text{C}$ .

EDS mapping analysis was performed to obtain information on the phase composition and microstructure of the sintered pellets. The elemental mapping of C1\_pellet shows that each particle contains the starting elements (Cr, Mn, Fe, Co, and Ni) (Figure 6b) and that their distribution is almost uniform and homogeneous since their contents vary slightly from one particle to another. The Cr content varies from 19.13 to 20.85 wt. %; the Mn content swings between 21.17 and 27.36 wt. %; Fe content changes from 18.88 to 20.62 wt. %; Co varies from 15.35 to 19.84 wt. % and Ni content varies from 15.59 to 19.06 wt. %. However, the distribution of Fe, Cr, Co, Mn, Ni, and Al in the C2\_pellet is inhomogeneous, as shown by the elemental mapping analysis in Figure 6c. Therefore, FeCr-rich powder particles with the composition of  $\text{Fe}_{40.46}\text{Cr}_{24.87}\text{Co}_{16.03}\text{Mn}_{7.68}\text{Al}_{10.96}$  can be related to BCC solid solution, CoAl-rich and CoNi-rich regions with compositions close, respectively, to  $\text{Co}_{41.46}\text{Al}_{25.13}\text{Fe}_{12.65}\text{Cr}_{6.9}\text{Ni}_{10.25}\text{Mn}_{3.61}$  and  $\text{Co}_{77.42}\text{Fe}_{4.44}\text{Cr}_{4.8}\text{Ni}_{3.75}\text{Mn}_{4.28}\text{Al}_{5.32}$  can be associated with the FCC solid solution. Those observations agree well with the XRD results.

### 3.3. Magnetic and Mechanical Properties

Magnetic properties, including coercivity, saturation magnetization, and squareness ratio, can be important for HEAs in various functional applications, such as in magnetic sensors, actuators, magnetic memory devices, and electromagnetic interference (EMI) shielding due to their excellent mechanical strength and ductility. Understanding the magnetic properties of HEAs is essential in realizing their multifunctional capabilities and can aid in the development of new HEA compositions with tailored magnetic properties for specific applications.

The hysteresis loops of the mechanically alloyed C1 and C2 powders for 24 exhibit sigmoidal shapes (Figure 7a) and comparable values of the saturation magnetization, coercivity, and squareness ratio, as shown in Table 5. The saturation magnetization represents the maximum magnetic moment per unit volume for a given substance that can be reached when all its atomic or molecular magnetic moments are aligned in the same direction with an external magnetic field. The magnetization reaches a maximum value that depends on its intrinsic properties, such as its chemical composition and crystal structure. Therefore, the reduced  $M_s$  values ( $M_s = 28.45 \text{ emu/g}$ ) of the C2 and C1 powders ( $M_s = 24.2 \text{ emu/g}$ ) can be mainly attributed to the formation of the FCC solid solutions.

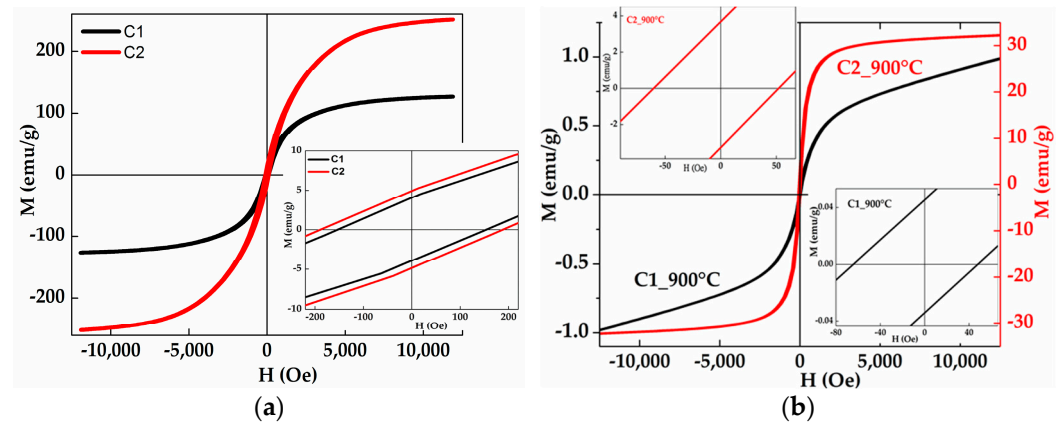


**Figure 7.** (a) Hysteresis loops of the mechanically alloyed C1 and C2 for 24 h; (b) C1\_900 °C and C2\_900 °C. Insets show the enlargement of the central parts.

**Table 5.** Saturation magnetization,  $M_s$ , coercivity,  $H_c$ , remanence,  $M_r$ , and squareness ratio of the mechanically alloyed and heat-treated powders.

Sample	$M_s$ (emu/g)	$H_c$ (Oe)	$M_r$ (emu/g)	$M_r/M_s$
C1	24.20	153.62	3.995	0.165
C1_900 °C	0.99	56.10	0.039	0.039
C2	28.45	188.48	4.897	0.172
C2_900 °C	32.28	56.18	3.471	0.107

The coercivity refers to the magnetic field strength required to reduce the magnetization to zero after the magnetic material has been magnetized to magnetic saturation. The coercivity is an extrinsic property that can be affected by the microstructure (crystallite size, particle size, particle morphology, grain boundaries, etc.) and crystal defects such as vacancies, interstitials, and dislocations. The values of  $H_c$  (153–188.48 Oe) can be due to the important amount of structural defects that are induced into the powder particles during the milling process. Thus, the produced powders have semi-hard magnetic behavior. The squareness ratio  $M_r/M_s$  is a dimensionless quantity between 0 and 1 that measures how square the loop is.  $M_r/M_s$  is used to characterize how a material retains its magnetization when the external magnetic field is removed. It provides information regarding whether particles are multiple magnetic domains ( $M_r/M_s < 0.1$ ), pseudo-single domains ( $0.1 < M_r/M_s < 0.5$ ), or single magnetic domains (SMD) ( $M_r/M_s > 0.5$ ). According to the  $M_r/M_s$  ratio values, which are about 0.165 and 0.172 for C1 and C2, respectively, the mechanically alloyed HEAs are pseudo-single domains [46].

For the heat-treated powders in the DSC (C1\_900 °C and C2\_900 °C), the M-H curves show different behaviors (Figure 7b). The inserts show the enlargement of the central parts. The magnetic behavior of the HEAs (ferromagnetism, paramagnetism, and antiferromagnetism) depends on their constituent elements, the specific ratios of those elements, their structural characteristics, and temperatures. Consequently, the shape of the hysteresis cycle can be influenced by the crystal structure, microstructure, phase constitution, and chemical composition. As can be seen, the C1 powders exhibit a paramagnetic behavior ( $M_s = 0.99$  emu/g and  $H_c = 56.10$  Oe) that can be related to the arrangement of the magnetic Fe, Co, and Ni atoms in addition to the formation of a single FCC solid solution. However, the C2 powders show a ferromagnetic character where  $M_s$  increases slightly to 32.28 emu/g, and the coercivity decreases to 56.18 Oe. The ferromagnetic behavior of the C2 powders can be due to either the BCC solid solution and/or the Co-rich sigma phase. The reduction in the coercivity of the heat-treated C1\_900 °C and C2\_900 °C powders can be related to the recovery and strain relaxation.

The hysteresis cycles of C1\_900 °C and C2\_900 °C, at room temperature, are not symmetric about the origin. They display a negative horizontal shift and a positive vertical shift. The horizontal H-axis shift can be related to an exchange bias (EB) behavior that can be due to the development of mixed antiferromagnetic (AF) and ferromagnetic (FM) interactions due to the presence of NiMn precipitates enriched in Ni and Mn and depleted in the other elements. Exchange bias behavior is typically observed in certain magnetic materials, such as antiferromagnetic (AFM) and ferromagnetic (FM) systems at lower temperatures. The exchange bias phenomenon is related to the exchange anisotropy created at the interface between AFM and FM regions and can be ascribed to the formation of an FM unidirectional anisotropy at the interface between different magnetic phases. Furthermore, the welding process produces equiaxed particle formation during the milling process. The values of  $E_B$  and coercivity field are calculated using  $H_E = -(H_1 + H_2)/2$  and  $H_c = |H_1 - H_2|/2$ , respectively, where  $H_1$  and  $H_2$  are the left and right field values at zero magnetization. Hence, both C1\_900 °C and C2\_900 °C powders exhibit the same value of coercivity ( $H_c = 56$  Oe), while  $H_E$  values are 8.21 and 4.15 Oe for C1 and C2, respectively. The reduction in the  $E_B$  value for the C2 powders might be due to the substitution of Al for Mn. The EB behavior at room temperature is not a common phenomenon, as HEAS alloys are usually not associated with traditional magnetic behavior.

The mechanical properties of the C1\_pellet and C2\_pellet were studied using microindentation tests under a 5 N load. Microindentation tests are relevant for studying mechanical properties at small scales because they provide valuable data on hardness, elastic modulus, plasticity, etc. Microindentation tests involve applying a controlled force or load to a sharp indenter (typically a diamond-pointed tip) and measuring the depth or displacement of the indenter into the material as a function of time. The resistance to plastic deformation might be attributed to the lattice distortion effect in HEAs since it breaks the perfect crystal structure and affects the mechanical properties. Furthermore, the presence of Al contributes directly/intrinsically to the microstructural evolution of the alloy through the solid solution and/or precipitation hardening. The Vickers microhardness decreases with Al addition from 584.85 Hv for the C1\_pellet to 522.65 Hv for the C2\_pellet. This behavior can be linked to the reduction in the relative density from 98% for the C1\_pellet to 86.4% for the C2\_pellet. The relative density of the HEAs was calculated with the formula  $\rho_1/\rho_0$ , where  $\rho_1$  is the actual density and  $\rho_0$  is the calculated theoretical density for the HEAs alloys. The reduction in the relative density can be attributed to the work hardening of the powders after 24 h of milling time. Furthermore, the higher values of the Vickers microhardness can be attributed to the crystallite size refinement, which plays an important role in the strengthening. Indeed, smaller crystallites have a higher density of grain boundaries, which impede dislocation motion, making it harder for them to move through the material. As a result, the material becomes harder with decreasing crystallite size. Likewise, the change in microhardness may be attributed to the microstructure inhomogeneity, structural hardening, and lattice distortion. The presence of different phases in the material with a finer dispersed second phase can affect microhardness values. Similarly, grain orientation and lattice defects (vacancies, dislocations, and stacking faults) create localized stress fields that hinder the motion of dislocations, making it more difficult for them to traverse the crystal lattice. As a result, materials with higher densities of defects tend to have higher microhardness values. Moreover, the microhardness values can be ascribed to the coexistence of BCC and FCC structures since hardness values of the as-cast HEAs, mainly with the FCC phase, are generally low at room temperature [47,48]. The wide variation in the HEAs hardness from 140 to 900 Hv has been related to the alloy systems and processing methods. For example, different microhardness values were obtained for the CoCrFeMnNi: 300 Hv for the prepared HEA alloy by casting [48], 336 Hv with a grain size of 100 nm [47], and 587 Hv for the prepared alloy by MA and high-pressure sintering (HPS) [47]. Moreover, the increase in the microhardness values of the as-cast CoCrFeMnNi and Al<sub>0.5</sub>CoCrFeMnNi HEAs alloys from 160 Hv and 175 Hv to 308.5 Hv and 314 Hv,

respectively, after ultrasonic impact treatment was attributed to the refined microstructures and precipitation strengthening mechanisms [49].

#### 4. Conclusions

MA was employed to produce FeCoCrNiMn (C1) and FeCoCrNiMn<sub>0.1</sub>Al<sub>0.1</sub> (C2) HEAs. The mechanically alloyed powders were subjected to continuous heating/cooling up to 900 °C/25 °C (C1\_900 °C and C2\_900 °C) and sintering at 500 °C for 1 h (C1\_pellet and C2\_pellet). The effect of Al addition on the phase formation, phase stability, and magnetic and mechanical properties was investigated using XRD, SEM, DSC, VSM, and microindentation. The main conclusions were as follows:

1. The crystal structure of both the C1 and C2 powders consists of BCC + FCC phases;
2. A mixture of BCC + FCC was observed for the C1\_pellet and BCC + FCC +  $\sigma$ -CrCo phases for the C2\_pellet;
3. The heat-treated powders to 900 °C exhibit a single FCC phase for the C1\_900 °C and a mixture of BCC + FCC +  $\sigma$ -CrCo for the C2\_900 °C powders;
4. The crystallite sizes of the C1, C2, C1\_pellet, C1\_900 °C, and C2\_900 °C are in the range of 6–93 nm;
5. The C1 and C2 powders exhibit a ferromagnetic behavior ( $M_s = 24.2$  emu/g and  $H_c = 153.62$  Oe) and C2 ( $M_s = 28.45$  emu/g and  $H_c = 188.48$  Oe) powders;
6. The C1\_900 °C powders show a paramagnetic behavior ( $M_s = 0.99$  emu/g and  $H_c = 56.10$  Oe);
7. The C2\_900 °C powders exhibit a ferromagnetic character with  $M_s = 32.28$  emu/g and  $H_c = 56.18$  Oe;
8. Both C1\_900 °C and C2\_900 °C HEAs alloys show an exchange bias ( $E_B$ ) behavior at room temperature. The  $E_B$  value is influenced by the Mn content;
9. The Vickers microhardness values are 584.85 Hv for the C1\_pellet and 522.65 Hv for the C2\_pellet;
10. This study reveals that MA and sintering at 500 °C for 1 h can be used as an effective way to produce HEA alloys with higher microhardness values. The produced HEA alloys exhibit comparable characteristics in terms of structure, microstructure, mechanical, and magnetic properties.

**Author Contributions:** Conceptualization, S.A.; methodology, S.A.; software, S.A.; validation, S.A. and J.J.S.; formal analyses, S.A.; investigation, H.H. and A.B.; resources, S.A.; data curation, S.A.; writing—original draft preparation, S.A.; writing—review and editing, S.A.; visualization, J.J.S.; supervision, S.A.; project administration, S.A. and J.J.S. All authors have read and agreed to the published version of the manuscript.

**Funding:** This research received no external funding.

**Data Availability Statement:** The data presented in this study are available on request from the corresponding author.

**Acknowledgments:** Financial support from The Directorate-General for Scientific Research and Technological Development (DGRSDT), MESRS Algeria, and Erasmus+ KA107 are acknowledged. The authors thank Foued KHAMMACI from the LM2S Laboratory for XRD, VSM, and DSC measurements.

**Conflicts of Interest:** The authors declare no conflict of interest.

#### References

1. Raja, R.K.; Sinha, S.K. Synthesis and phase investigation of equiatomic AlCrFeMnNi alloys dispersed with partially stabilized zirconia for nuclear applications. *Mater. Sci. Forum* **2020**, *978*, 145–151. [CrossRef]
2. Li, W.; Xie, D.; Li, D.; Zhang, Y.; Gao, Y.; Liaw, P.K. Mechanical behavior of high-entropy alloys. *Prog. Mater. Sci.* **2021**, *118*, 100777. [CrossRef]
3. Li, Z.; Zhao, S.; Ritchie, R.O.; Meyers, M.A. Mechanical properties of high-entropy alloys with emphasis on face-centered cubic alloys. *Prog. Mater. Sci.* **2019**, *102*, 296–345. [CrossRef]

4. Wu, Y.; Zhang, F.; Yuan, X.; Huang, H.; Wen, X.; Wang, Y.; Lu, Z. Short-range ordering and its effects on mechanical properties of high-entropy alloys. *J. Mater. Sci. Technol.* **2021**, *62*, 214–220. [CrossRef]
5. Onawale, O.T.; Cobbinah, P.V.; Nzeukou, R.A.; Matizamhuka, W.R. Synthesis route, microstructural evolution, and mechanical property relationship of high-entropy alloys (HEAs): A review. *Materials* **2021**, *14*, 3065. [CrossRef] [PubMed]
6. Konakoglou, K.; Mathiou, C.; Georgatis, E.; Georganakakis, K.; Karantzas, A.E. (FeMnNi)<sub>84</sub>(AlTi)<sub>16</sub> High-Entropy Alloy: Correlation of Microstructure, Strengthening Mechanisms and Hardness at Various Conditions (As-Cast, Solution Treated, Aged). *Metallogr. Microstruct. Anal.* **2022**, *11*, 309–326. [CrossRef]
7. Ma, L.; Gao, Z.; Hu, S.; Zeng, Z.; Xu, J.; Wang, J. Effect of cooling rate on microstructure and mechanical properties of Al<sub>0.3</sub>CoCrFeNi high-entropy alloy. *Mater. Res. Express* **2019**, *6*, 056540. [CrossRef]
8. Rogal, L. Semi-solid processing of the CoCrCuFeNi high entropy alloy. *Mater. Des.* **2017**, *119*, 406–416. [CrossRef]
9. Rajendrachari, S. An overview of high-entropy alloys prepared by mechanical alloying followed by the characterization of their microstructure and various properties. *Alloys* **2022**, *1*, 116–132. [CrossRef]
10. Avila-Rubio, M.A.; Baldenebro-Lopez, J.A.; Soto-Rojo, R.; Ceballos-Mendivil, L.G.; Garza-Montes-de-Oca, N.F.; Baldenebro-Lopez, F.J. Effect of Mo and Ti on the microstructure and microhardness in AlCoFeNiMoTi high entropy alloys prepared by mechanical alloying and conventional sintering. *Adv. Powder Technol.* **2020**, *31*, 1693–1701. [CrossRef]
11. Qiu, Z.; Yao, C.; Feng, K.; Li, Z.; Chu, P.K. Cryogenic deformation mechanism of CrMnFeCoNi high-entropy alloy fabricated by laser additive manufacturing process. *Int. J. Lightweight Mater. Manuf.* **2018**, *1*, 33–39. [CrossRef]
12. Huang, W.; Hou, J.; Wang, X.; Qiao, J.; Wu, Y. Excellent room-temperature tensile ductility in as-cast Ti<sub>37</sub>V<sub>15</sub>Nb<sub>22</sub>Hf<sub>23</sub>W<sub>3</sub> refractory high entropy alloys. *Intermetallics* **2022**, *151*, 107735. [CrossRef]
13. Jien-Wei, Y.E.H. Recent progress in high entropy alloys. *Ann. Chim. Sci. Mat* **2006**, *31*, 633–648.
14. Kumar, N.; Tiwary, C.S.; Biswas, K. Preparation of nanocrystalline high-entropy alloys via cryomilling of cast ingots. *J. Mater. Sci.* **2018**, *53*, 13411–13423. [CrossRef]
15. Zhao, Y.Y.; Nieh, T.G. Correlation between lattice distortion and friction stress in Ni-based equiatomic alloys. *Intermetallics* **2017**, *86*, 45–50. [CrossRef]
16. Cao, L.; Wang, X.; Wang, Y.; Zhang, L.; Yang, Y.; Liu, F.; Cui, Y. Microstructural evolution, phase formation and mechanical properties of multi-component AlCoCrFeNi<sub>x</sub> alloys. *Appl. Phys. A* **2019**, *125*, 699. [CrossRef]
17. Lu, Y.; Gao, X.; Jiang, L.; Chen, Z.; Wang, T.; Jie, J.; Kang, H.; Zhang, Y.; Guo, S.; Ruan, H.; et al. Directly cast bulk eutectic and near-eutectic high entropy alloys with balanced strength and ductility in a wide temperature range. *Acta Mater.* **2017**, *124*, 143–150. [CrossRef]
18. Kumar, J.; Kumar, N.; Das, S.; Gurao, N.P.; Biswas, K. Effect of Al addition on the microstructural evolution of equiatomic CoCrFeMnNi alloy. *Trans. Indian Inst. Met.* **2018**, *71*, 2749–2758. [CrossRef]
19. Mohanty, S.; Maity, T.N.; Mukhopadhyay, S.; Sarkar, S.; Gurao, N.P.; Bhowmick, S.; Biswas, K. Powder metallurgical processing of equiatomic AlCoCrFeNi high entropy alloy: Microstructure and mechanical properties. *Mater. Sci. Eng. A* **2017**, *679*, 299–313. [CrossRef]
20. Joseph, J.; Stanford, N.; Hodgson, P.; Fabijanic, D.M. Understanding the mechanical behaviour and the large strength/ductility differences between FCC and BCC Al<sub>x</sub>CoCrFeNi high entropy alloys. *J. Alloys Compd.* **2017**, *726*, 885–895. [CrossRef]
21. Wei, F.; Wei, S.; Lau, K.B.; Teh, W.H.; Lee, J.J.; Seng, H.L.; Ramamurthy, U. Compositionally graded Al<sub>x</sub>CoCrFeNi high-entropy alloy manufactured by laser powder bed fusion. *Materialia* **2022**, *21*, 101308. [CrossRef]
22. Tian, Q.W.; Zhang, G.J.; Yin, K.X.; Cheng, W.L.; Wang, Y.N.; Huang, J.C. Effect of Ni content on the phase formation, tensile properties and deformation mechanisms of the Ni-rich AlCoCrFeNi<sub>x</sub> (x = 2, 3, 4) high entropy alloys. *Mater. Charact.* **2021**, *176*, 111148. [CrossRef]
23. Wang, Y.P.; Li, B.S.; Ren, M.X.; Yang, C.; Fu, H.Z. Microstructure and compressive properties of AlCoCrFeNi high entropy alloy. *Mater. Sci. Eng. A* **2008**, *491*, 154–158. [CrossRef]
24. Manzoni, A.; Daoud, H.; Volkl, R.; Glatzel, G.; Wanderka, N. Phase separation in equiatomic AlCoCrFeNi high-entropy alloy. *Ultramicroscopy* **2013**, *132*, 212–215. [CrossRef]
25. Wang, W.R.; Wan, W.L.; Wang, S.C.; Tsai, Y.C.; Lai, C.H.; Yeh, J.W. Effects of Al addition on the microstructure and mechanical property of Al<sub>x</sub>CoCrFeNi high-entropy alloys. *Intermetallics* **2012**, *26*, 44–51. [CrossRef]
26. Lutterotti, L. MAUD Program Version 2.992. Available online: <https://maud.radiographema.com/> (accessed on 28 November 2021).
27. Rietveld, H.M. The Rietveld method. *Phys. Scr.* **2014**, *89*, 098002. [CrossRef]
28. Vaidya, M.; Pradeep, K.G.; Murty, B.S.; Wilde, G.; Divinski, S.V. Bulk tracer diffusion in CoCrFeNi and CoCrFeMnNi high entropy alloys. *Acta Mater.* **2018**, *146*, 211–224. [CrossRef]
29. Takeuchi, A.; Inoue, A. Classification of bulk metallic glasses by atomic size difference, heat of mixing and period of constituent elements and its application to characterization of the main alloying element. *Mater. Trans.* **2005**, *46*, 2817–2829. [CrossRef]
30. Xing, Y.; Li, C.J.; Mu, Y.K.; Jia, Y.D.; Song, K.K.; Tan, J.; Eckert, J. Strengthening and deformation mechanism of high-strength CrMnFeCoNi high entropy alloy prepared by powder metallurgy. *J. Mater. Sci. Technol.* **2023**, *132*, 119–131. [CrossRef]
31. Otto, F.; Dlouhý, A.; Pradeep, K.G.; Kuběňová, M.; Raabe, D.; Eggeler, G.; George, E.P. Decomposition of the single-phase high-entropy alloy CrMnFeCoNi after prolonged anneals at intermediate temperatures. *Acta Mater.* **2016**, *112*, 40–52. [CrossRef]

32. He, J.Y.; Liu, W.H.; Wang, H.; Wu, Y.; Liu, X.J.; Nieh, T.G.; Lu, Z.P. Effects of Al addition on structural evolution and tensile properties of the FeCoNiCrMn high-entropy alloy system. *Acta Mater.* **2014**, *62*, 105–113. [[CrossRef](#)]
33. Zhang, Y.; Zuo, T.T.; Tang, Z.; Gao, M.C.; Dahmen, K.A.; Liaw, P.K.; Lu, Z.P. Microstructures and properties of high-entropy alloys. *Prog. Mater. Sci.* **2014**, *61*, 1–93. [[CrossRef](#)]
34. Mizutani, U. *Hume-Rothery Rules for Structurally Complex Alloy Phases*; CRC Press: Boca Raton, FL, USA, 2016.
35. He, Q.F.; Ye, Y.F.; Yang, Y. Formation of Random Solid Solution in Multicomponent Alloys: From Hume-Rothery Rules to Entropic Stabilization. *J. Phase Equilib. Diffus.* **2017**, *38*, 416–425. [[CrossRef](#)]
36. Wu, Z.; Bei, H.; Otto, F.; Pharr, G.M.; George, E.P. Recovery, Recrystallization, Grain Growth and Phase Stability of a Family of FCC-Structured Multi-component Equiatomic Solid Solution Alloys. *Intermetallics* **2014**, *46*, 131–140. [[CrossRef](#)]
37. Zhang, Y.; Zhou, Y.J.; Lin, J.P.; Chen, G.L.; Liaw, P.K. Solid-Solution Phase Formation Rules for Multi-component Alloys. *Adv. Eng. Mater.* **2008**, *10*, 534–538. [[CrossRef](#)]
38. Ye, Y.F.; Wang, Q.; Lu, J.; Liu, C.T.; Yang, Y. High-Entropy Alloy: Challenges and Prospects. *Mater. Today* **2016**, *19*, 349–362. [[CrossRef](#)]
39. Guo, W.; Li, J.; Qi, M.; Xu, Y.; Ezatpour, H.R. Effects of heat treatment on the microstructure, mechanical properties and corrosion resistance of AlCoCrFeNiTi<sub>0.5</sub> high-entropy alloy. *J. Alloys Compd.* **2021**, *884*, 161026. [[CrossRef](#)]
40. Christofidou, K.; Pickering, E.; Orsatii, P.; Mignanelli, P.; Slater, T.; Stone, H.; Jones, N. On the influence of Mn on the phase stability of the CrMnxFeCoNi high entropy alloys. *Intermetallics* **2018**, *92*, 84. [[CrossRef](#)]
41. Wang, X.J.; Xu, M.; Liu, N.; Liu, L.X. The formation of sigma phase in the CoCrFeNi high-entropy alloys. *Mater. Res. Express* **2021**, *8*, 076514. [[CrossRef](#)]
42. He, W.; Zeng, C.; Yang, W.; Chen, W.; Ai, Y. Impact of different Cr contents on microstructural evolution and mechanical behaviour of CoCr<sub>x</sub>CuFeMnNiV high-entropy alloys. *J. Mater. Res. Technol.* **2022**, *21*, 4577. [[CrossRef](#)]
43. Chung, D.H.; Liu, X.D.; Yang, Y. Fracture of sigma phase containing Co–Cr–Ni–Mo medium entropy alloys. *J. Alloys Compd.* **2020**, *846*, 156189. [[CrossRef](#)]
44. Wang, S.; Chen, L.; Li, Q.; Wang, S.; Wu, M.; Yang, S.; Xiang, D. Effects of Al or Mo Addition on Microstructure and Mechanical Properties of Fe-Rich Nonequiatomic FeCrCoMnNi High-Entropy Alloy. *Metals* **2022**, *12*, 191. [[CrossRef](#)]
45. Yukawa, N.; Hida, M.; Imura, T.; Kawamura, M.; Mizuno, Y. Structure of chromium-rich Cr-Ni, Cr-Fe, Cr-Co, and Cr-Ni-Fe alloy particles made by evaporation in argon. *Metall. Mater. Trans. B* **1972**, *3*, 887. [[CrossRef](#)]
46. Alleg, S.; Hamza, L.; Ibrir, M.; Souilah, S.; Tebib, W.; Fenineche, N.E.; Greneche, J.M. Microstructural, hyperfine, and magnetic properties of FeSiBCuNb deposits. *J. Supercond. Nov. Magn.* **2015**, *28*, 2431. [[CrossRef](#)]
47. Yu, P.F.; Zhang, L.J.; Cheng, H.; Zhang, H.; Ma, M.Z.; Li, Y.C.; Li, G.; Liaw, P.K.; Liu, R.P. The high-entropy alloys with high hardness and soft magnetic property prepared by mechanical alloying and high-pressure sintering. *Intermetallics* **2016**, *70*, 82. [[CrossRef](#)]
48. Cantor, B.; Chang, I.T.H.; Knight, P.; Vincent, A.J.B. Microstructural development in equiatomic multicomponent alloys. *Mater. Sci. Eng. A* **2004**, *375*, 213. [[CrossRef](#)]
49. Li, M.; Zhang, Q.; Han, B.; Song, L.; Li, J.; Yang, J. Investigation on microstructure and properties of Al<sub>x</sub>CoCrFeMnNi high entropy alloys by ultrasonic impact treatment. *J. Alloys Compd.* **2020**, *816*, 152626. [[CrossRef](#)]

**Disclaimer/Publisher’s Note:** The statements, opinions and data contained in all publications are solely those of the individual author(s) and contributor(s) and not of MDPI and/or the editor(s). MDPI and/or the editor(s) disclaim responsibility for any injury to people or property resulting from any ideas, methods, instructions or products referred to in the content.